Alexandria Engineering Journal 112 (2025) 281–292

Contents lists available at ScienceDirect

Alexandria Engineering Journal

journal homepage: www.elsevier.com/locate/aej

Original article

Investigation of support structure configurations for selective laser melting of In718

Yi Nie [a,b,*], Chenlong Xu [a,b], Zhongkui Liu [a], Lihang Yang [a], Tianqi Li [b], Yinfeng He [a,b,c]

[a] Nottingham Ningbo China Beacons of Excellence Research and Innovation Institute, University of Nottingham Ningbo China, Ningbo, Zhejiang 315100, PR China
[b] Faculty of Science and Engineering, University of Nottingham Ningbo China, Ningbo, Zhejiang 315100, PR China
[c] Faculty of Engineering, University of Nottingham, Nottingham NG7 2RD, UK

ARTICLE INFO

Keywords:
Selective laser melting
Support structure
In 718
Deformation
Residual stress

ABSTRACT

The Selective Laser Melting (SLM), as a widely used metallic Additive manufacturing (AM) process, relies heavily on support structures. This study investigated the impact of different support structure configurations on the quality of In718 samples fabricated through SLM. On the basis of a comprehensive review of existing support structures configurations from the literature, three typical configurations: block, cone, and lattice, were designed to support cantilever parts for performance comparison. A coupled thermo-structural finite element simulation using ANSYS was performed to evaluate the temperature, deformation, and thermal stress evolution during the printing process of the three supported cantilever structures. The residual stress and deformation of the printed In718 cantilevers with different support structures were measured for validation. The results showed that block support exhibits the best strength and heat dissipation capability, making it the most effective support configuration for the SLM of In718 material. This research provides a fundamental procedure for evaluating the supporting performances among various support structures for the SLM process.

1. Introduction

Additive Manufacturing (AM), commonly known as 3D printing, is recognized as a revolutionary manufacturing technique of the 21st century [1]. Among the various AM methods. Selective Laser Melting (SLM) stands out as one of the most widely used for producing strong, nearly fully dense metal components [2]. The SLM of Inconel 718 (In718), a high-performance nickel-based superalloy, is increasingly important in industries such as aerospace and power generation due to its exceptional mechanical properties and resistance to high-temperature environments [3]. However, a key challenge in the SLM process of In718 is the lack of optimized support structures, which are crucial for maintaining part integrity during printing and post-processing.

In SLM process support structures are essential for anchoring and supporting overhanging and horizontal features as shown in Fig. 1a. These supports are critical in controlling part distortion and preventing collapse during the build. Moreover, the high thermal gradients inherent in SLM generate significant residual stresses, which are mitigated by support structures that aid in heat dissipation, improving surface quality and reducing warping [4]. However, excessive support use increases build time, material wastage, and post-processing requirements [5]. Therefore, an effective support structure must be robust enough to maintain integrity during construction, minimize part distortions, and reduce post-processing needs and material consumption. Unlike other materials such as stainless steel, aluminium alloy, or titanium alloy, In718 exhibits unique thermal and mechanical behaviour. Its higher melting point, lower thermal conductivity, and greater tensile strength make heat management and support structure design particularly different [6]. Additionally, In718 is difficult to machine, which further complicates the support removal phase compared to these other alloys [7].

Various support configurations have been utilized in 3D printing, as shown in Fig. 1b and c [8]. The tree [9], 'Y' [10], and unit cell [11] supports exhibit poor heat dissipation, leading to localized heat concentration and elevated thermal stress. Conversely, block support configurations are particularly significant in the SLM process. Calignano [4] conducted a Taguchi L_{36} experiment to optimize block supports by adjusting hatching, teeth height, and teeth base interval, aiming to reduce deformation and collapse in aluminium and titanium alloy overhanging structures. Cao *et al.* [12] investigated additional criteria

* Corresponding author at: Nottingham Ningbo China Beacons of Excellence Research and Innovation Institute, University of Nottingham Ningbo China, Ningbo, Zhejiang 315100, PR China.
E-mail address: yi-nie@nottingham.edu.cn (Y. Nie).

https://doi.org/10.1016/j.aej.2024.11.006
Received 25 May 2024; Received in revised form 27 September 2024; Accepted 1 November 2024
Available online 5 November 2024

Nomenclature

T	Instantaneous temperature
$K(T)$	Temperature-dependent thermal conductivity of the material
$H(T)$	Temperature-dependent enthalpy
F	Heat flux
t	time;
Ts	solidus temperature
T_l	liquidus temperature
ρ	density
C_p	specific heat capacity
L_f	latent heat of fusion
T_0	room temperature,
$\Delta\varepsilon_{ij}^{e}$	elastic strain increment
$\Delta\varepsilon_{ij}^{th}$	thermal strain increment
$\Delta\varepsilon_{ij}^{p}$	plastic strain increment.
D_{ijlm}	elastic stiffness tensor
E	Young's modulus
ν	Poisson's ratio
δ	Dirac delta function
α	thermal expansion coefficient
ΔT	temperature increments
A	real projected contact area
A_{nom}	nominal projected contact area
c^2	ratio of real projected contact area to the nominal projected contact area
P	the testing load
$\sigma(\varepsilon_{repr} + \varepsilon_{res})$	flow stress
ε_{repr}	effective plastic strain
ε_{res}	von Mises residual strain

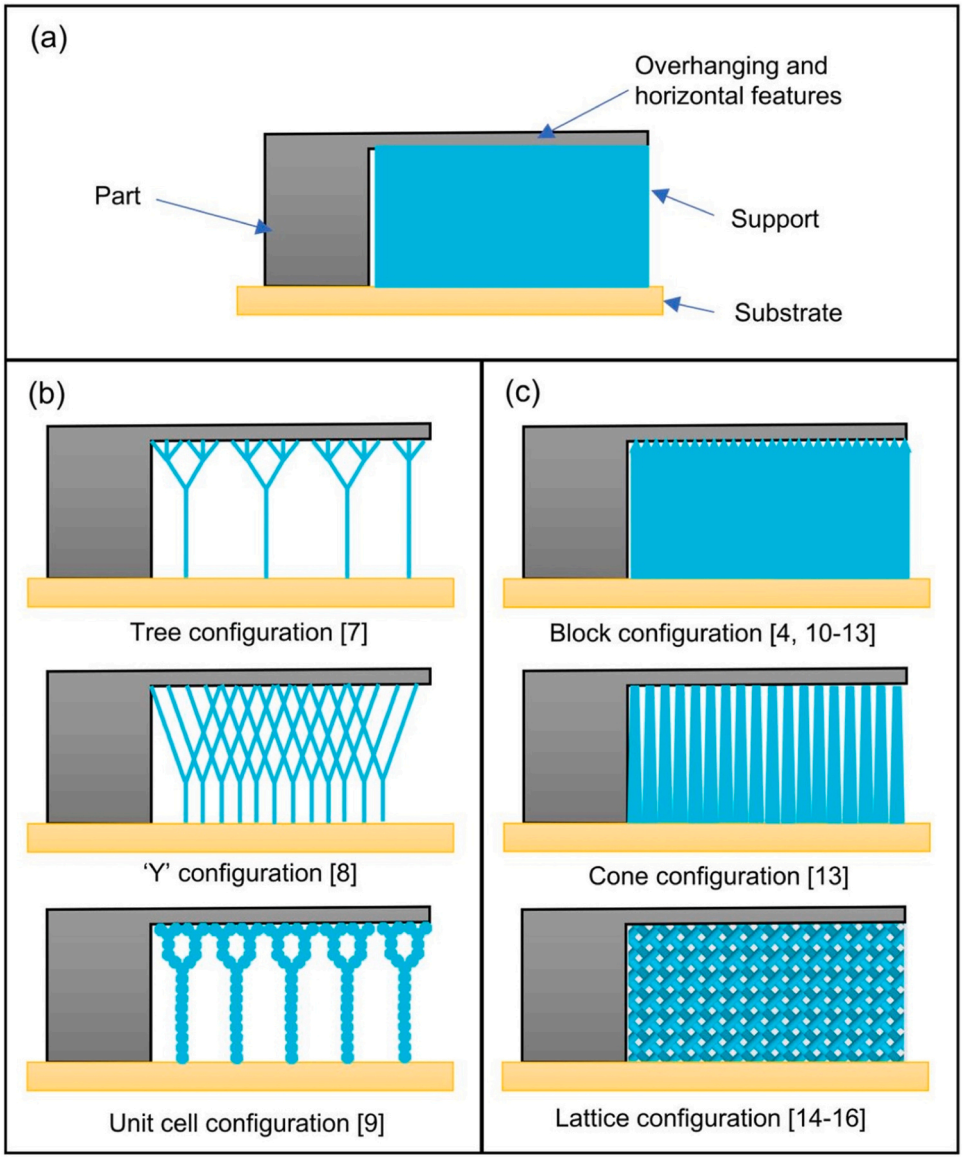

Fig. 1. a) shows a schematic of overhanging structures, where supports are typically needed during printing; various types of supports explored in the literature include: b) tree, 'Y,' and unit cell supports; and c) popular block, cone, and lattice supports for SLM.

affected by block supports and building angles, including dimensional accuracy, surface roughness, Vickers microhardness, residual stress, and even the microstructure of printed maraging steel MS1 parts. Poyraz *et al.* [13] performed a series of experiments to explore the effect of different design parameters on block supports, such as hatch distance, fragmentation, tooth top length, and Z offset, providing valuable insights for optimizing block support designs. To visualize the function of block support structures, Cooper *et al.* [14] applied long cantilever structures during their experiments, while Cao *et al.* [15] compared block and cone supports in terms of ease of removal through both experiments and simulations.

Recently, lattice support configurations have gained attention due to their advantage of a low solid volume fraction. Lattice structures such as the 'Schwartz,' 'Gyroid,' and 'Diamond' were experimentally compared by Kladovasilakis *et al.* [16], with the Diamond structure demonstrating the best mechanical properties. Hao *et al.* [17] further verified the processability of the Diamond support, investigating the effect of cell size on the manufacturability of the structure. Hussein *et al.* [18] applied Diamond and Gyroid lattice structures as supports for titanium alloy cantilever builds, studying the effects of volume fractions and cell size on support manufacturability, support volume, and fabrication time. They found that lattice supports with very low volume fractions, up to 8 %, could be constructed, significantly reducing the amount of material used for support.

This study aims to systematically investigate the performance of support configurations previously applied to other materials in the context of In718, contributing to a better understanding of the impact of support design on the overall quality and efficiency for the SLM In718 parts. Three typical support configurations – block, cone, and lattice – will be selected and designed for a cantilever setup for performance investigation, as shown in Fig. 1c. Both computational simulations and experimental validation will be performed to compare the three kinds of supports with respect to deformation, residual stress, surface quality, ease of support removal, and material usage, ultimately determining the optimal support structure configuration.

2. Methodologies

2.1. Support design

Three support configurations were analysed for their effects on deflection, stress, material usage, surface roughness, and post-processing in the SLM process of In718 alloy. The block support, known for easy construction, the cone support with its conical design for easy removal, and the lattice support favoured in additive manufacturing for its efficient heat paths and simple powder removal, were selected and shown in Fig. 2b-d. The diamond was selected to represent the lattice structure in this research on the basis of previous studies [16].

A cantilever part was chosen to assess support performance due to its large overhanging structure, shown in Fig. 2a. The deformation of long cantilever arms can be easily measured, which gives a visual indication on the performance of the support structure. To ensure that the material usage for the three supports was the same, their volume fraction was set to 30 %. The wall thickness of the block support is set at 0.2 mm and the sides length of the square grid is 1.4 mm. The top and bottom radius of the cone support are 0.5 mm and 0.8 mm, respectively. The distance between the bottom of the cones were set to 0.5 mm. The cell size of the diamond support was set as 6 mm. The contacts between block, cone, and diamond supports and substrates were calculated to be 38 %, 62.5 %, and 19 %, respectively.

2.2. Computational simulation

In this research, the macroscale (mm) modelling was considered, which involves thermal or energy sources applied over large representative volume elements to calculate residual stresses in the part and determine distortion or build failure.

2.2.1. Governing equations

a) Thermal analysis

According to Kamara et al. [19], the adopted general heat conduction equation is expressed as follows:

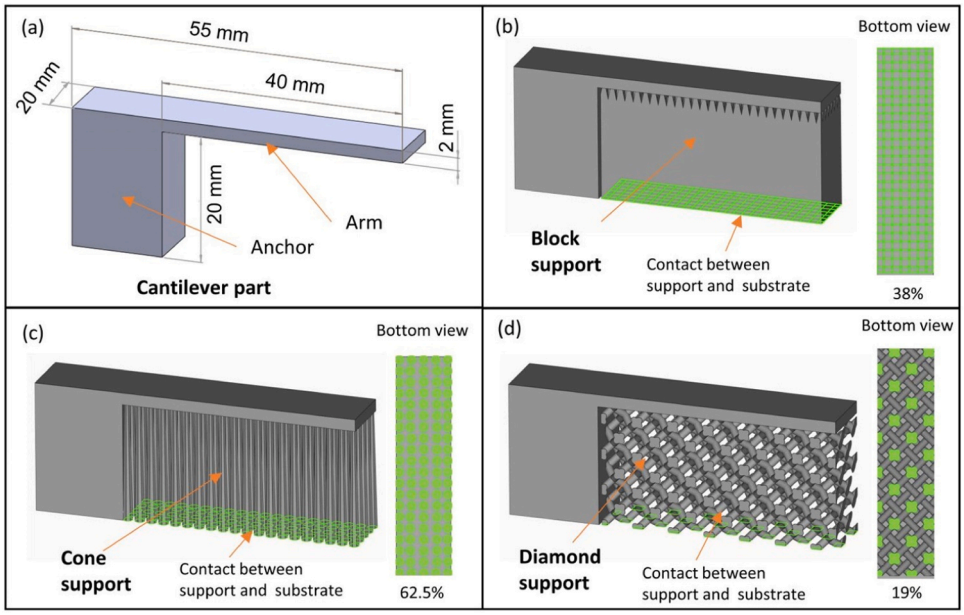

Fig. 2. a) Dimensions of the overhanging cantilever structure; and selected support designs used in this work: b) block support configuration, c) cone support configuration, and d) diamond support configuration.

$$K(T) \bullet \left(\frac{\partial^2 T}{\partial x^2}+\frac{\partial^2 T}{\partial y^2}+\frac{\partial^2 T}{\partial z^2}\right)+F=\frac{\partial H(T)}{\partial t} \tag{1}$$

where $K(T)$ is the temperature-dependent thermal conductivity of the material; T is instantaneous temperature; F is the heat flux, t is time in seconds; x, y and z are the directions in space. $H(T)$ is a temperature-dependent enthalpy, which accounts for the latent heat evolution of the process due to phase change effects,

For $T \le T_s$

$$H(T)=\rho\int_{T_0}^{T} C_p dT \tag{2}$$

For $T_s \le T \le T_l$

$$H(T)=\rho\int_{T_0}^{T_s} C_p dT+\rho L_f\left(\frac{T-T_s}{T_l-T_s}\right) \tag{3}$$

And for $T > T_l$

$$H(T)=\rho\int_{T_0}^{T_s} C_p dT+\rho L_f+\rho\int_{T_l}^{T} C_p dT \tag{4}$$

where T_l is liquidus temperature, T_s is solidus temperature, ρ is density, C_p is the specific heat capacity, L_f is the latent heat of fusion, and T_0 is room temperature, which is assumed as 22°C.

b) Structural analysis

The structural analysis calculates the residual stresses resulting from strains due to expansion and contraction caused by temperature changes and inelastic strains from plasticity. The total incremental strain vector can be expressed as a superposition of elastic, thermal and plastic components in the form of

$$\Delta\varepsilon_{ij}^{tol}=\Delta\varepsilon_{ij}^{e}+\Delta\varepsilon_{ij}^{th}+\Delta\varepsilon_{ij}^{p} \tag{5}$$

where $\Delta\varepsilon_{ij}^{e}$ is the elastic strain increment, $\Delta\varepsilon_{ij}^{th}$ is the thermal strain increment, $\Delta\varepsilon_{ij}^{p}$ is the plastic strain increment.

The resulting stress increment is given by the elastic strain increment, $\Delta\varepsilon_{ij}^{e}$ through

$$\Delta\sigma_{ij}=D_{ijlm}\Delta\varepsilon_{ij}^{e} \tag{6}$$

where D_{ijlm} is the elastic stiffness tensor given by Hooke's law as

$$D_{ijlm}=\frac{E}{1+\nu}\left[\frac{1}{2}\left(\delta_{il}\delta_{jm}+\delta_{lm}\delta_{ij}\right)+\frac{\nu}{1-2\nu}\delta_{ij}\delta_{lm}\right] \tag{7}$$

where δ is a Dirac delta function, E is Young's modulus, and ν is Poisson's ratio.

Combining Eqs. (5) and (6) yields

$$\Delta\sigma_{ij}=D_{ijlm}(\Delta\varepsilon_{ij}^{tol}-\Delta\varepsilon_{ij}^{th}-\Delta\varepsilon_{ij}^{p}) \tag{8}$$

where $\Delta\varepsilon_{ij}^{th}=\alpha\delta_{lm}\Delta T$, and α and ΔT are thermal expansion coefficient and temperature increments, respectively.

2.2.2. Numerical setup

As it takes enormous computational time to simulate the entire printing process based on a true scan situation, some reasonable simplifications can be applied. The actual deposited powder layers are aggregated into a finite element "super layer", which is added by the "element birth" technique and heated all at once. Each "super layer" is originally set to melt temperature instead of applying heat flux. The dissipation of the part to the surrounding powder is modelled using convective boundary conditions.

With the above assumptions, the simulation can be conducted in two consecutive stages because the thermal and structural physics are largely uncoupled. The first stage is a layer-by-layer transient thermal analysis. The second stage is a transient structural analysis, using the temperature field determined by the previous thermal analysis as a load to calculate the corresponding residual stresses.

Cartesian mesh was generated in this simulation shown in Fig. 3. As severe thermal gradients were expected to occur in parts and supports, fine meshes are required. The mesh size for the support and cantilever part is set to 0.2 mm, whereas that for the substrate with dimensions of 100 × 50 × 10 mm is set to 2 mm. The total element number is 1002,007, 944,196, and 917,083 for block, cone and diamond support cases, respectively. To facilitate data mapping, the structural analysis uses the same mesh as the thermal analysis, but with modified element and material properties.

Inconel 718 was chosen as the deposition material, whose material properties are shown in Fig. 4. The temperature-dependent material properties of the material are adopted. The standard processing parameters were suggested by BLT Ltd., where the laser scan speed is 700 mm/s, hatch spacing is 0.1 mm, laser power is 500 W, layer thickness is 0.02 mm and interval time between each layer is 10 s.

Instead of applying a heat flux, each 'super layer' is initially set to the melting temperature of 1260°C during the building process. The preheat temperature of metal powder is set at 70 °C. The cooled bottom face of the substrate is set at room temperature of 22 °C. The top surface of the build is assumed to contact with the gas of 22° C under a convection coefficient of 1×10^{-5} W/mm^2·°C. The other surfaces of the geometry are assumed to contract with powder of 70 °C under a convection coefficient of 2×10^{-6} W/mm^2·°C. The cooling process was also analyzed after building. The thermal analysis will be terminated with the maximum temperature of the build reaches room temperature.

In the simulation of the AM process, the model evolves over time by turning on each element layers using standard element birth and death techniques to simulate the material deposition process. In addition, associated boundary conditions such as thermal convection surfaces will also evolve. When all element layers have been added, the build step is complete. The commercial finite element package of ANSYS Workbench was applied to predict the thermal and structural behavior of the In718 cantilever with different support structures during the SLM process.

2.3. Experimental validation

The sample preparation process is shown in Fig. 5. The printing process was carried out using a BLT S200 SLM machine whose maximum laser out-put power is 500 W, process precision is 100–200 μm, Optical precision is 50 μm diameter beam, max processing size is 105 × 105 × 200 mm, and the In718 cantilevers together with different support structures were printed for experimental validation. The cantilevers with designed three kinds of support structures were printed one substrate. In718 is supplied and fed onto the building substrate layer-by-layer. The building chamber and peripherals connected were flooded with N_2 gas. Standard processing parameters mentioned in Section 2.2.2 are applied to print the samples. The final samples after powder cleaning are shown in Fig. 4(d).

The height at different positions on the cantilever was measured to indicate the deflection of the cantilever shown in Fig. 6a. Five positions were measured using a Vernier calliper for each part, each position was measured five times and the average value was calculated.

To measure and quantify the residual stresses in SLM parts, methods such as neutron diffraction, crack compliance method, bridge curvature method and Vickers micro-indentation have been utilized [20]. Compared to other methods, the Vickers micro-indentation method is simple and fast. Assuming the residual stress is an equal-biaxial state in the horizontal plane, the uniaxial stress-strain curve obeys a power-law function: $\sigma(\varepsilon_p) = K{\varepsilon_p}^n$. The tensile stress-strain curve of In718 alloys fabricated by SLM and the power-low fitted curved was measured by Lu

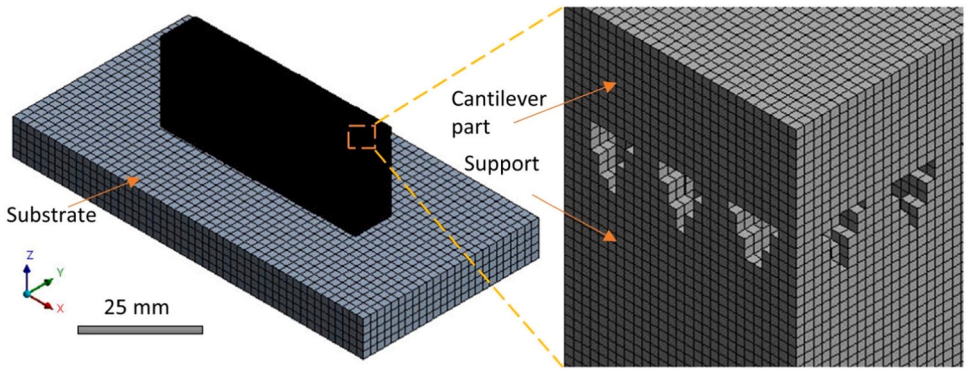

Fig. 3. The finite element model used for computational simulation of the SLM process, illustrated with block support.

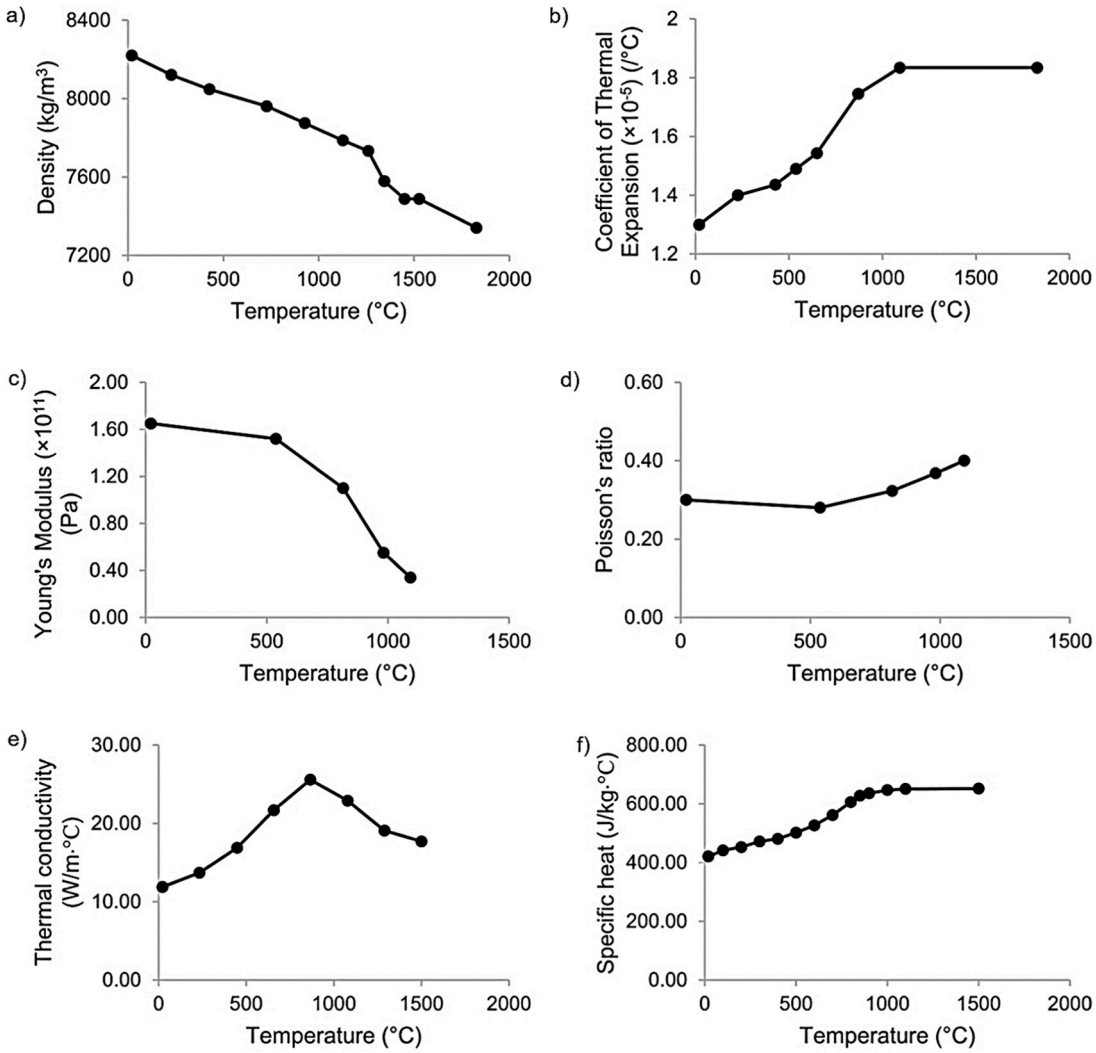

Fig. 4. The key material properties of In718 (temperature dependent) used in this model include: a) density, b) coefficient of thermal expansion, c) Young's modulus, d) Poisson's ratio, e) thermal conductivity, and f) specific heat.

et al. indicating that $K = 1355.82$, and $n = 0.15$. According to Carlsson and Larsson [21,22], the von Mises residual stress σ_{res} and residual strain ε_{res} follow the relations:

$$H = C\sigma(\varepsilon_{repr} + \varepsilon_{res}) \tag{9}$$

$$c^2 = c_0^2 - 0.32\ln[1 + \frac{\sigma_{res}}{\sigma(\varepsilon_{res})}] \tag{10}$$

where H is the microhardness of the test point, and $H = P/A$ (P is the testing load). C is a material constant, and $C = 3$ [22]. $\sigma(\varepsilon_{repr} + \varepsilon_{res})$ is the flow stress. ε_{repr} is the effective plastic strain, and $\varepsilon_{repr} = 0.08$ [22]. c^2 is the ratio of real projected contact area A (mm^2) to the nominal projected contact area A_{nom} (mm^2), and $c^2 = A/A_{nom}$. c_0^2 is the corresponding value for the case of zero residual stress, and $c_0^2 \approx 1$ [20].

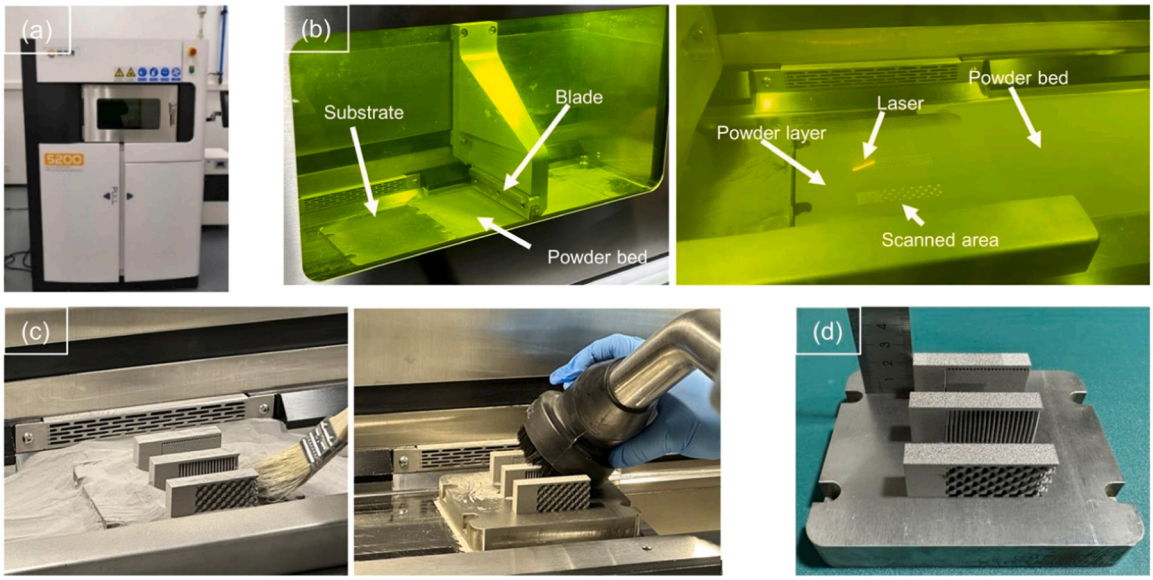

Fig. 5. illustrates the sequence for fabricating cantilever parts with different supports using an a) SLM machine BLT-S200: b) In718 powder feeding and melting process; c) de-powdering process after printing; and d) the appearance of the fabricated cantilevers with designed supports.

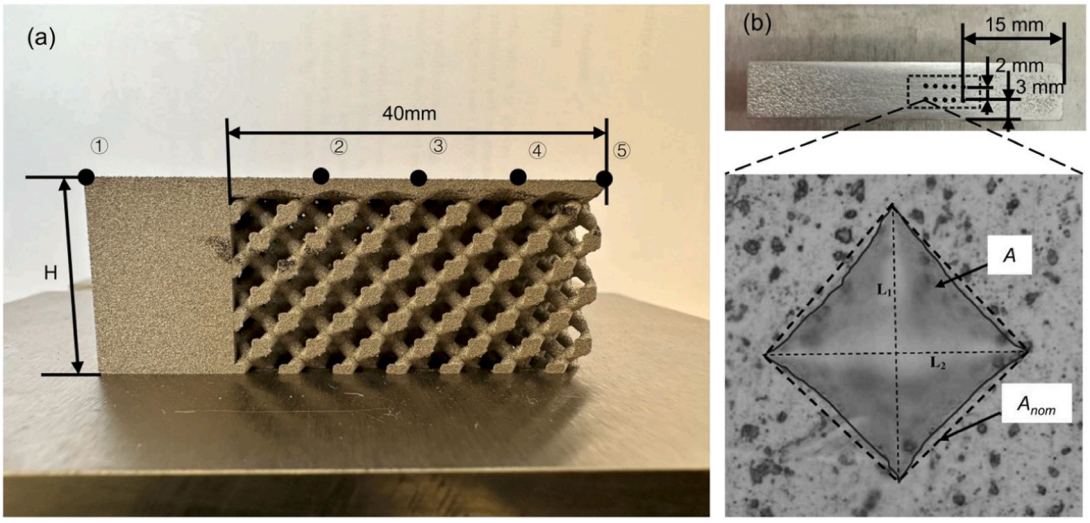

Fig. 6. Characterization of deformation and residual stress in each printing part: a) locations where deformation measurements were performed (Diamond support for illustration) and b) Schematic of test point in Vickers hardness measurement (top view).

The real projected contact area A could be measured from the hardness tester directly, and the nominal projected contact area A_{nom} was calculated with the diagonal lines (L_1 and L_2) of indentation, shown in Fig. 6b:

$$A_{nom} = [L_1 + L_2/2]^2 \Big/ 2 \tag{11}$$

The residual stress can be calculated by the formulas:

$$\varepsilon_{res} = \left(\frac{H}{CK}\right)^{\frac{1}{n}} - \varepsilon_{repr} \tag{12}$$

$$\sigma_{res} = K{\varepsilon_{res}}^{n} \times [e^{\frac{c_0^2 - c^2}{0.32}} - 1] \tag{13}$$

The raw surface of the samples was too rough for the Vickers hardness testing, post-processing is required. 1200 grid sandpapers were used to polish the upper surface of the cantilever until the surface became smooth. The experiment was carried out by the Universal Hardness Tester, with a load of 49 N and a 10 s contact time. Each sample was tested at 10 points adjacently to obtain the average value. Fig. 6b and c show the testing points on the top surface of printed cantilever parts and the projected contact areas during Vickers hardness testing, respectively.

3. Results and discussion

3.1. Temperature field analysis

The simulation includes both build-up and cooling down processes during the SLM process of cantilevers with the three different kinds of support. Fig. 7 shows the temperature field of the building process, which could be divided into three stages: the anchor and support building stage (Fig. 7a), cantilever arm building stage (Fig. 7b), and cooling down stage (Fig. 7c). During the anchor and support building stage, the temperature of the built support is found lower than the cantilever anchor as less heat is applied and accumulated in the loose

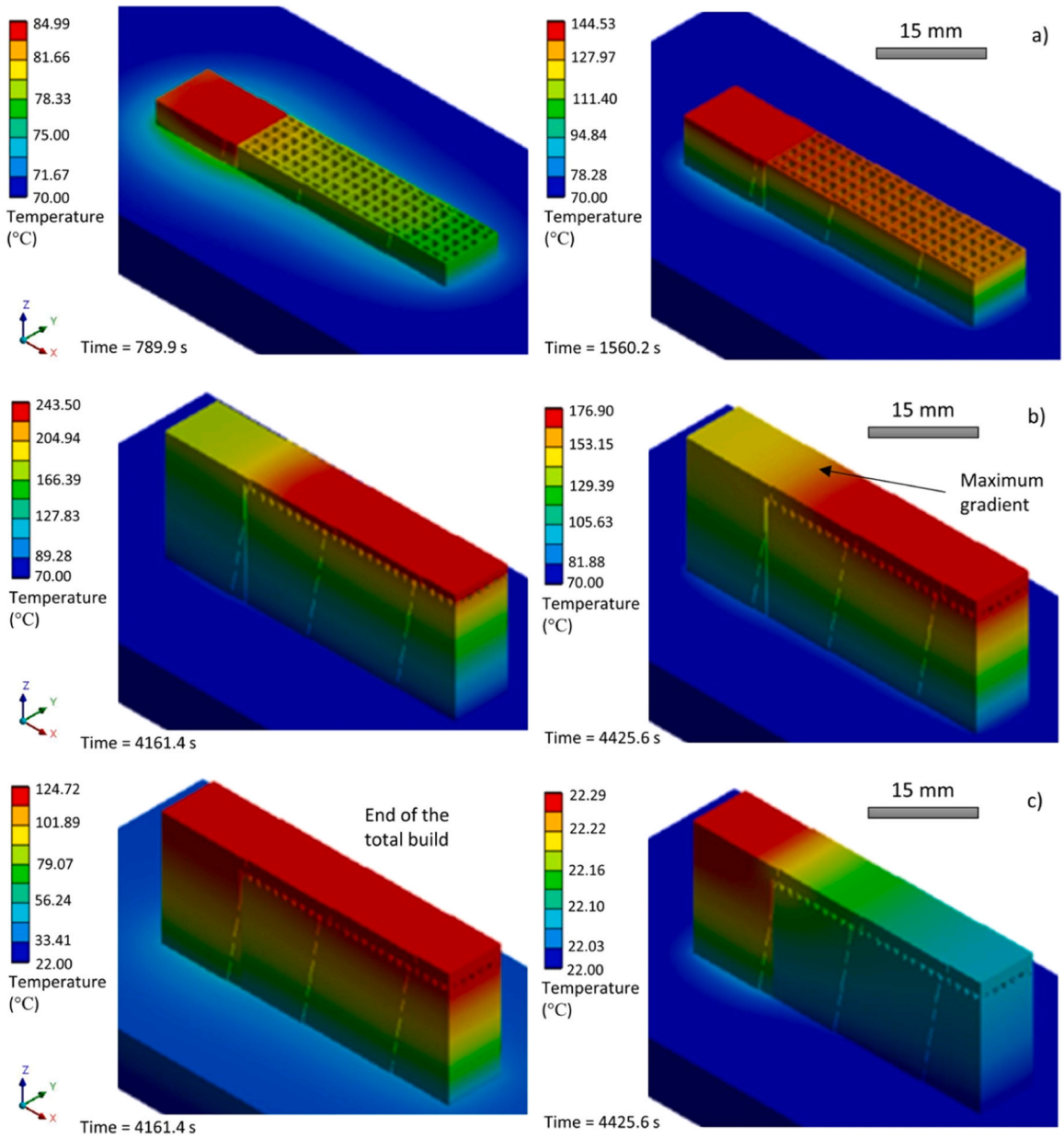

Fig. 7. Temperature field history throughout the cantilever building process in SLM process (block support configuration): a) anchor and support building step, b) cantilever arm building step, and c) cooling step.

support structure by the laser beam. Though the interval time is applied to allow the cooldown of material between each layer, the maximum temperature after each layer is found to increase gradually which indicates that the heat will accumulate during the whole deposition process. During the cantilever arm building stage, the maximum temperature and temperature gradient are found on the top surface of the cantilever. More heat accumulation is found in the cantilever arm compared to the anchor due to the difficulty of transferring heat downward by the underneath loose support structure. The temperature gradient will exist between the cantilever arm and anchor as well as the cantilever arm and support. In the cooling down stage, the heat accumulated in the cantilever arm is found to dissipate slower than that in the cantilever anchor, which results in the temperature gradient existing between them. The maximum temperature of the part is close to the room temperature at the end which demonstrates that the cooling time and cooling condition are efficient.

The temperature field at the end of the cantilever arm building step will directly affect the afterwards cooling process of heat transfer pattern and generation of residual stress. The comparison of the temperature field at that time point with different support structures is depicted in Fig. 8 and Table 1. It demonstrates that both the maximum temperature and temperature gradient of the cantilever with block support are the lowest, which indicates that the block support has the best heat dissipation abilities. The heat dissipation capacity of the block support is due to its evenly distributed grid and small gaps, which allow heat to be transferred evenly downwards through the thermal paths. The maximum temperature and temperature gradient of the cantilever with cone support are 12.9 % and 19 °C/m higher than those of the part with block support, respectively. It indicates that the thermal performance of cone support is slightly worse than that of the block support. The diamond support results in the highest maximum temperature and temperature gradient in the cantilever, which demonstrates that the diamond support has the lowest heat dissipation performance. This is because the area of the contact surface between the support and cantilever or substrate is small (shown in Fig. 2), which causes slow heat dissipation. In addition, the maximum temperature gradient occurs at

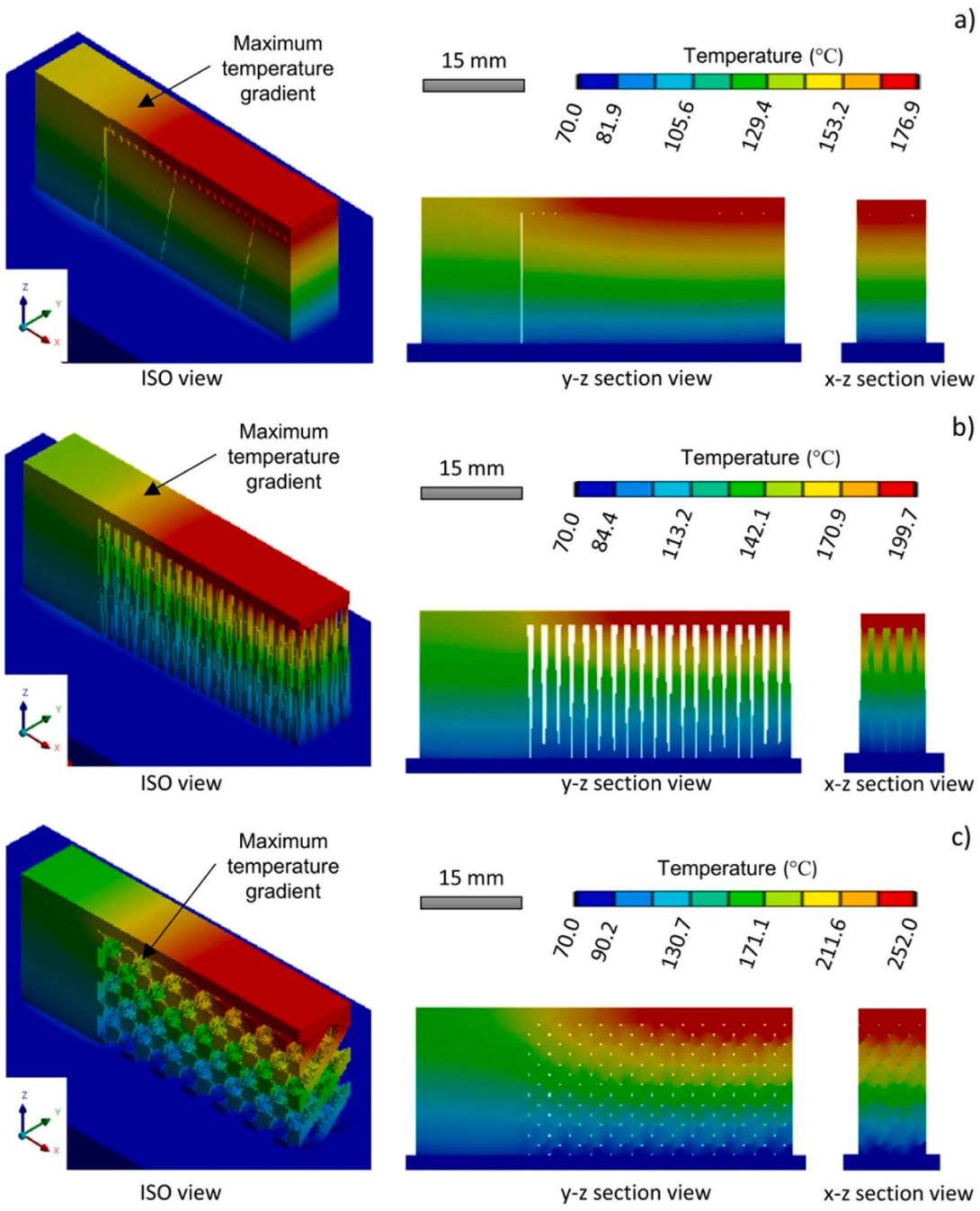

Fig. 8. Temperature field of the built cantilever with a) lock support configuration, b) cone support configuration, c) diamond support configuration at the end of the cantilever arm building.

Table 1
Maximum temperature and temperature gradient of the cantilevers with block, cone, and diamond supports at the end of the cantilever arm building step.

Support configuration	Maximum temperature (°C)	Maximum temperature gradient (°C/m)
Block	176.8	31
Cone	199.7	50
Diamond	252.0	88

the intersection between the cantilever arm and the anchor for the block and cone supports, while that for the diamond support happens in between the cantilever arm and support structure.

3.2. Deformation field analysis

The repeat thermal expansion and contraction will lead to severe deformation of the build during the SLM process, which not only affects the dimension accuracy of the part but also increases the potential collision between the build and the powder blade. The simulated and experimental deformation of the cantilevers with different support structures after cooling down are shown in Fig. 9. The maximum deflection was observed at the location which is furthest away from the cantilever. This is the weak point where warpage normally happens during the SLM process. The maximum deflections for the parts with block, cone, and diamond supports are 0.297, 1.562, and 1.041 mm, respectively, which indicates that the block supports are stronger than the other two supports to prevent deflection during the In718 material

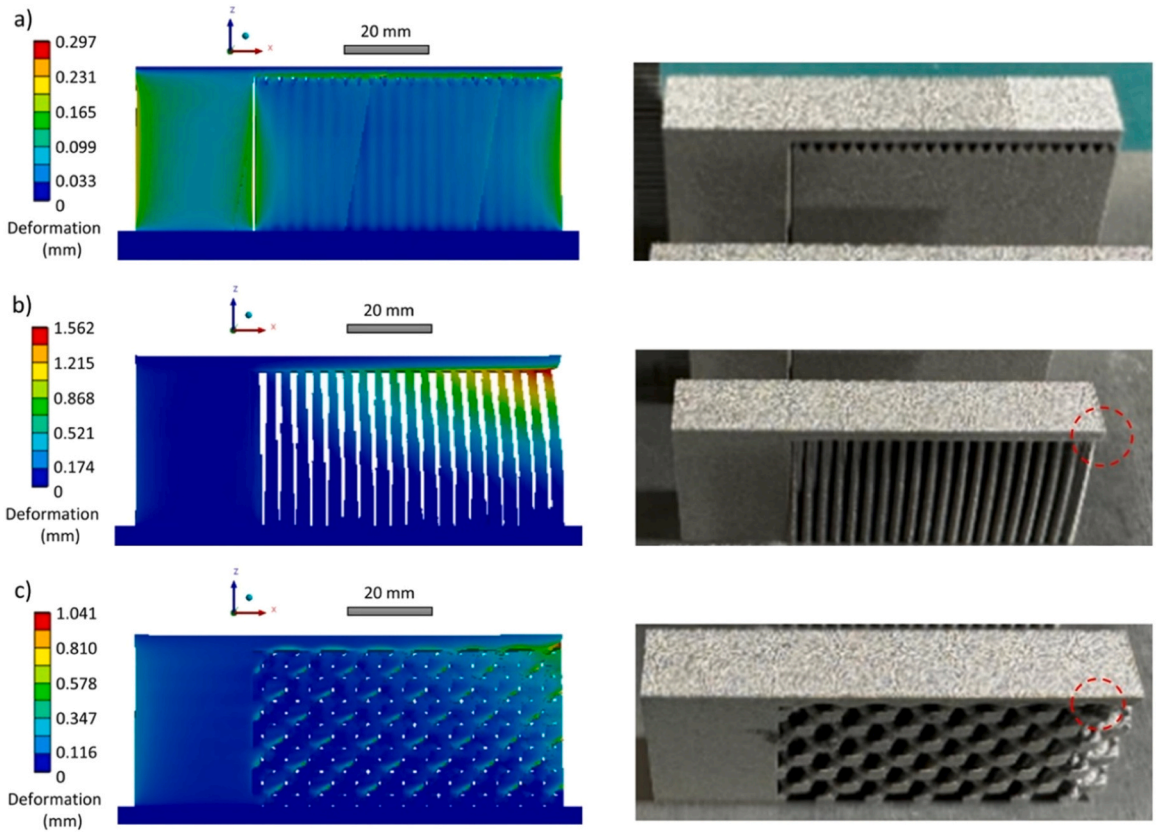

Fig. 9. Comparison of simulation and experimental deformation of the built cantilevers: a) block support configuration, b) cone support configuration, and c) diamond support configuration.

deposition process. The block support consists both the vertical construction to resist the upward warping and horizontal uniform grid to withstand the lateral forces, while the cone support includes only independent vertical cones that can neither share excessive stresses nor withstand lateral forces. In addition, the unsupported area of the cantilever with diamond support is significantly larger than the those with the other two supports, where significant warping occurs under the cantilever arm.

The deflections on the top surfaces of the cantilevers, which are directly related to the final dimension, are focused on and analysed. The deflection at testing point 5 (shown in Fig. 6a), which is more visible, was chosen for the comparison between simulation and experimental results, shown in Table 2. In both simulation and experimental results, the deflection of block-supported cantilever is the smallest and that of the cone-supported cantilever has the largest deflection, which demonstrates that block support performs the best in preventing the deformation of the printed cantilever. The measured deflections are found 30 % larger than the simulated ones. This is because the surface of the sample is not sufficiently post-processed, the surface is coarse and there is a gap between the measuring instrument and the real surface.

Table 2
The simulation and experimental deflections at the testing point 5 (shown in Fig. 6a).

Support configuration	Deflection at testing point 5 (mm)	
	Simulation	Experiment
Block	0.0023	0.03
Cone	0.225	0.16
Diamond	0.078	0.10

3.3. Stress field analysis

Severe residual stress will be accumulated during the rapid heating and cooling SLM process, where plastic deformation, cracking or delamination of the build will easily happen. The residual stress field of the build with different support structures after cooling down is shown in Fig. 10. The maximum residual stresses for all three supports occur at the contact between the support and the part. Higher residual stresses were observed inside the cantilever arm rather than the anchor, which is evidence that the heat dissipation capacity of all the support structures is worse than that of the cantilever anchor. The maximum residual stresses for block, cone and diamond-supported cantilevers are 1117.4 MPa, 1368.3 MPa, and 1247.9 MPa respectively. The comparison results demonstrate that block support performs the best to prevent residual stress generation during the SLM process. The result is consistent with the temperature field analysis as residual stress is mainly driven by temperature gradient [12]. The part with block support dissipates heat faster, leading to a small temperature gradient after the building step and small residual stress during the cooling down step. In addition, all the maximum residual stresses for the three supports are found exceeding the yield strength of the material, which indicates local plastic deformation is inevitable during the building process.

High residual stresses are also found distributed on the top surface of the cantilevers, especially at the junction between the cantilever arm and anchor. In this position, the residual stresses for block, cone and diamond supported cantilever are simulated as 801 MPa,755 MPa and 771 MPa, respectively, while the experimental measured residual stresses are 637.6 MPa, 591.3 MPa, and 609.4 MPa shown in Table 3. Both the experimental and simulation results indicate that the block-supported cantilever has the highest residual stresses on the top surface, while the cone support leads to the lowest residual stresses on the top surface of the cantilever beam. The difference is related to the

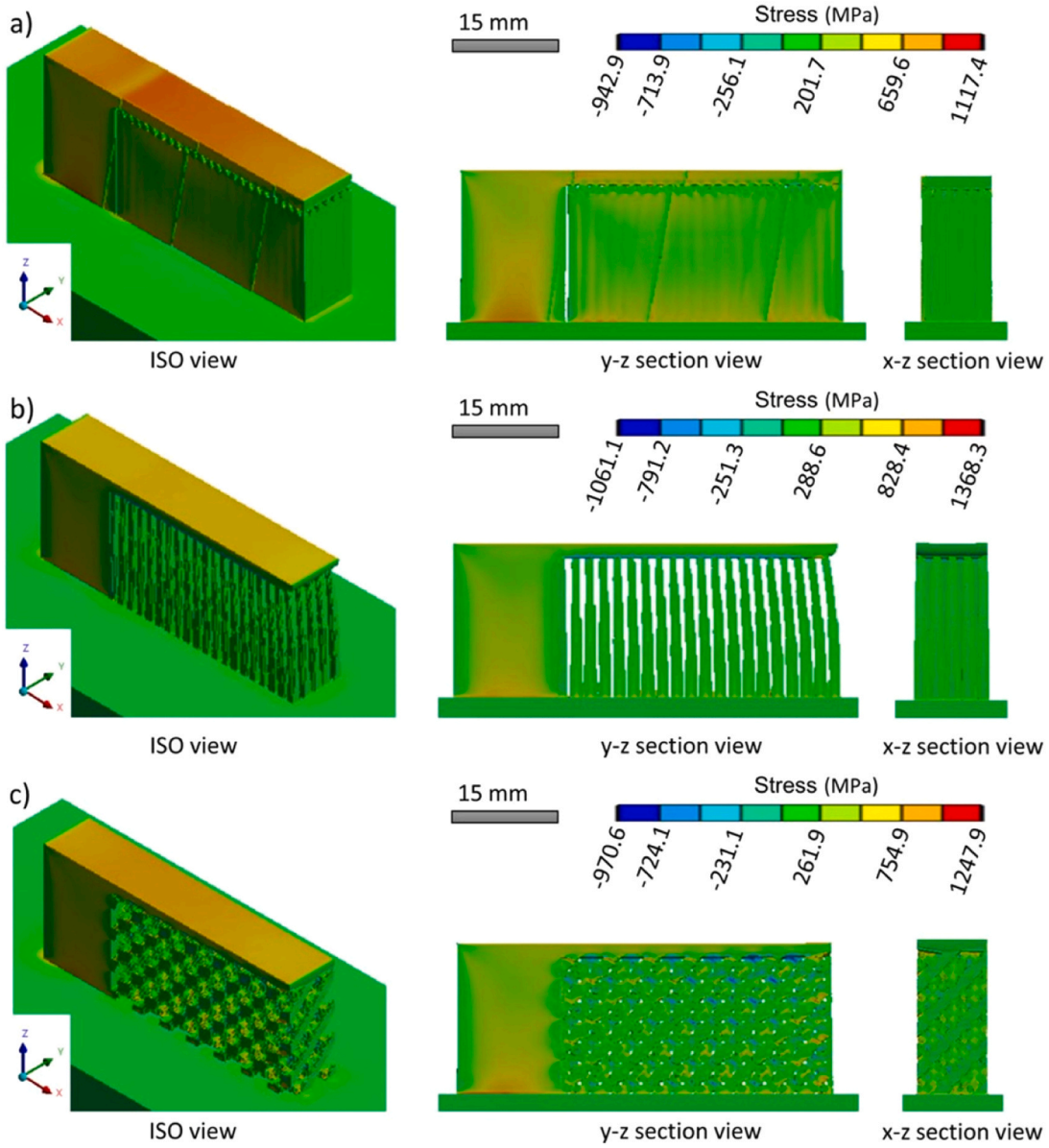

Fig. 10. Stress field of the built cantilevers at end of cooling down step: a) block support configuration, b) cone support configuration, and c) diamond support configuration.

Table 3
Average residual stresses on the top surfaces of the built cantilevers with block, cone, and diamond supports: simulation and experimental results comparison.

Support configuration	Residual stress on the upper surface (MPa)	
	Simulation	Experiment
Block	755	637.6
Cone	771	591.3
Diamond	252.0	609.4

contact surface between the support and the cantilever arm. The shape of the contact surface (shown in Fig. 2) is asymmetrical, and the large gaps between support surfaces lead to an uneven heat distribution. A larger local temperature gradient was then created and the residual stress increased for the parts with cone, diamond and block supports, sequentially. The simulated residual stresses are found to be higher than experimental results, which is mainly due to the grinding on the upper surface by 0.3 mm in thickness before testing. According to the existing research [23,24], the further away from the upper surface, the lower the residual stress. The grinding process releases some of the residual stresses, which makes the testing results smaller.

3.4. Performance comparison

The performance of support structures is influenced not only by deformation and stress during the material deposition process but also by material usage, surface roughness, and post-process difficulty. A summary of the performance comparison among the block, cone, and diamond supports for the SLM of In718 is presented in Table 4. The material usage for all three supports is controlled uniformly. Notably, the block support exhibits the smallest maximum deformation and residual stress compared to the other two supports. The surface roughness on the top surface of the cantilever parts was measured using the Keyence VR-5000 3D measurement system. The results indicate that the support configuration has little effect on the surface roughness of printed parts, which is mainly related to the local material flow in the micro molten pool. Both manual and machining methods can be applied for

Table 4
Performance comparison among the block, cone, and diamond support for the SLM of In718.

Support configuration	Block	Cone	Diamond
Maximum deformation (mm)	0.297	1.562	1.041
Maximum residual stress (MPa)	1117.4	1368.3	1247.9
Material usage (g)	19.13	19.13	19.13
Surface roughness Sa (μm)	22.88	25.66	20.38
Manual support removal	Difficult	Difficult	Difficult
Support removal by machining	1 cut	2 cuts	2 cuts

support removal. Manual removal is challenging and labour-intensive for all the three supports. In terms of machining via electrical discharge machining, one cut is needed for the block support as it only touches the cantilever arm. In contrast, two cuts are required for both the cone and diamond supports because they touch both the cantilever arm and anchor. This performance comparison highlights that the block support demonstrates the best supporting capability for the SLM of In718.

The previous studies have suggested that lattice support outperform block support [16–18], while the findings presented in this paper challenge that statement. Notably, prior research focused on the SLM of stainless steel and titanium alloys. In contrast, the investigation on In718 in this paper, including both computational and experimental tests, reveals that block support, previously considered less effective in the literature, actually provides superior performance during the SLM process. Thus, the design of support structures for SLM should be material-specific rather than universally applied.

4. Conclusion

This study compares the performance of three support configurations through both simulation and experimentation in the SLM of In718. While material usage and surface quality impacts remain consistent, the performance differences among the supports are summarized as follows:

- The block support exhibits the best supporting ability due to its uniform configuration both vertically and horizontally. It effectively dissipates heat, rapidly dispersing energy accumulated during the SLM process, which reduces warping and controls part shape. Additionally, it minimizes residual stress generation and facilitates easier support removal compared to the other supports.
- The cone support demonstrates good thermal performance but has the weakest mechanical strength. Although it provides even heat dissipation paths for the printed samples, its independent structure makes it vulnerable to excessive loads or lateral stresses, leading to potential bending and deformation.
- The diamond structure offers sufficient strength as a support but struggles with heat dissipation, primarily due to large unsupported areas that are susceptible to local plastic and thermal deformation.

The finite element model in this study can be extended for parametric studies to investigate how structural dimensions of the supports influence their performances. Future research could examine variations in thickness and gaps between layers for block supports. For cone supports, studies could focus on the diameters at both ends and the gaps between them, while lattice structures may be explored in terms of cell size and lattice type. Furthermore, the simulation model and experimental methods presented here have the potential to generate extensive datasets for artificial intelligence (AI) algorithms, enabling the identification of optimal support configurations and the prediction of performance outcomes [25]. Additionally, machine learning could be employed to facilitate real-time adjustments of support configurations during the SLM process through in-line monitoring, thereby enhancing both efficiency and part quality. Support structures could evolve to become smarter by integrating AI, offering greater precision and adaptability, ultimately leading to improved product outcomes.

CRediT authorship contribution statement

Yinfeng He: Writing – review & editing, Supervision, Software, Resources, Conceptualization. **Tianqi Li:** Writing – review & editing, Visualization. **Lihang Yang:** Writing – review & editing, Validation. **Zhongkui Liu:** Writing – review & editing, Validation. **Chenlong Xu:** Writing – review & editing, Writing – original draft, Project administration, Methodology, Investigation, Formal analysis, Data curation. **Yi Nie:** Writing – review & editing, Supervision, Software, Resources, Funding acquisition, Conceptualization.

Declaration of Competing Interest

The authors declare the following financial interests/personal relationships which may be considered as potential competing interests: Yi Nie reports financial support was provided by Nottingham Ningbo China Beacons of Excellence Research and Innovation Institute. If there are other authors, they declare that they have no known competing financial interests or personal relationships that could have appeared to influence the work reported in this paper.

Acknowledgements

The authors would like to acknowledge the support of the Nottingham Ningbo China Beacons of Excellence Research and Innovation Institute (I01220400001, I01220800006).

References

[1] E.M. Sefene, State-of-the-art of selective laser melting process: a comprehensive review, J. Manuf. Syst. 63 (2022) 250–274.
[2] D. Herzog, V. Seyda, E. Wycisk, C. Emmelmann, Additive manufacturing of metals, Acta Mater. 117 (2016) 371–392.
[3] E. Hosseini, V. Popovich, A review of mechanical properties of additively manufactured Inconel 718, Addit. Manuf. 30 (2019) 100877.
[4] F. Calignano, Design optimization of supports for overhanging structures in aluminum and titanium alloys by selective laser melting, Mater. Des. 64 (2014) 203–213.
[5] D. Thomas, The development of design rules for selective laser melting, Cardiff Metropolitan University, 2009.
[6] T. DebRoy, H.L. Wei, J.S. Zuback, T. Mukherjee, J.W. Elmer, J.O. Milewski, A. M. Beese, Ad Wilson-Heid, A. De, W. Zhang, Additive manufacturing of metallic components — process, structure and properties, Prog. Mater. Sci. 92 (2018) 112–224.
[7] G.R. Thellaputta, P.S. Chandra, C. Rao, Machinability of nickel based superalloys: a review, Mater. Today.: Proc. 4 (2017) 3712–3721.
[8] J. Jiang, X. Xu, J. Stringer, Support structures for additive manufacturing: a review, J. Manuf. Mater. Process. 2 (2018) 64.
[9] L. Zhu, R. Feng, J. Xi, P. Li, X. Wei, A lightweight design of tree-shaped support structures for SLM additive manufacturing, Comput. -Aided Des. Appl. 17 (2020) 716–726.
[10] M.X. Gan, C.H. Wong, Practical support structures for selective laser melting, J. Mater. Process. Technol. 238 (2016) 474–484.
[11] R. Vaidya, S. Anand, Optimum support structure generation for additive manufacturing using unit cell structures and support removal constraint, Procedia Manuf. 5 (2016) 1043–1059.
[12] Q. Cao, J. Zhang, S. Chang, J.Y.H. Fuh, H. Wang, The effect of support structures on maraging steel MS1 parts fabricated by selective laser melting at different building angles, Rapid Prototyp. J. 26 (2020) 1465–1476.
[13] Ö. Poyraz, E. Yasa, G. Akbulut, A. Orhangul and S. Pilatin, Investigation of support structures for direct metal laser sintering (DMLS) of IN625 parts, Proceedings of the solid freeform fabrication symposium, Austin, Texas, USA (2015) 560-574.
[14] K. Cooper, P. Steele, B. Cheng, K. Chou, Contact-free support structures for part overhangs in powder-bed metal additive manufacturing, Inventions 3 (2018) 2.
[15] Q. Cao, Y. Bai, J. Zhang, Z. Shi, J.Y.H. Fuh, H. Wang, Removability of 316L stainless steel cone and block support structures fabricated by Selective Laser Melting (SLM), Mater. Des. 191 (2020) 108691.
[16] N. Kladovasilakis, K. Tsongas, D. Tzetzis, Mechanical and FEA-assisted characterization of fused filament fabricated triply periodic minimal surface structures, J. Compos. Sci. 5 (2021) 58.
[17] L. Hao, D. Raymont, C. Yan, A. Hussein and P. Young, Design and additive manufacturing of cellular lattice structures, Proceedings of The International Conference on Advanced Research in Virtual and Rapid Prototyping (VRAP), Leiria (2011) 249-254.

[18] A. Hussein, L. Hao, C. Yan, R. Everson, P. Young, Advanced lattice support structures for metal additive manufacturing, J. Mater. Process. Technol. 213 (2013) 1019–1026.
[19] A. Kamara, S. Marimuthu, L. Li, A numerical investigation into residual stress characteristics in laser deposited multiple layer waspaloy parts, J. Manuf. Sci. Eng. 133 (2011) 031013.
[20] Y. Lu, S. Wu, Y. Gan, T. Huang, C. Yang, L. Junjie, J. Lin, Study on the microstructure, mechanical property and residual stress of SLM Inconel-718 alloy manufactured by differing island scanning strategy, Opt. Laser Technol. 75 (2015) 197–206.
[21] S. Carlsson, P.-L. Larsson, On the determination of residual stress and strain fields by sharp indentation testing.: Part I: theoretical and numerical analysis, Acta Mater. 49 (2001) 2179–2191.
[22] S. Carlsson, P.-L. Larsson, On the determination of residual stress and strain fields by sharp indentation testing.: Part II: experimental investigation, Acta Mater. 49 (2001) 2193–2203.
[23] Y. Liu, Y. Yang, D. Wang, A study on the residual stress during selective laser melting (SLM) of metallic powder, J. Adv. Manuf. Technol. 87 (2016) 647–656.
[24] B. Vrancken, V. Cain, R. Knutsen, J. Van Humbeeck, Residual stress via the contour method in compact tension specimens produced via selective laser melting, Scr. Mater. 87 (2014) 29–32.
[25] S.U. Khan, W. Jamshed, Finite element analysis and wear rate analysis of nano coated high speed steel tools for industrial application, Babylon. J. Mech. Eng. 2023 (2023) 13–19.